RESEARCH ARTICLE

A Mathematical Model to Study the Fundamental Functions of Phagocytes and Inflammatory Cytokines During the Bone Fracture Healing Process

Imelda Trejo,[a] Hristo V. Kojouharov,[b]

[a]Theoretical Biology and Biophysics (T-6), Information System and Modeling Groups (A-1), Los Alamos National Laboratory, Los Alamos, NM 87545, USA; [b]Department of Mathematics, The University of Texas at Arlington, Arlington, TX 76019-0408, USA

ABSTRACT

A mathematical model is presented to study the effects of phagocytes and inflammatory cytokines on bone fracture healing during the early stages of the process. The model incorporates the interactions among macrophages, mesenchymal stem cells, osteoblasts, inflammatory cytokines, and the cartilage and bone extracellular matrices. The resulting system of nonlinear ordinary differential equations is studied analytically and numerically. The stability analysis revealed that the excessive accumulation of phagocytes and inflammatory cytokines at the injury site can lead to unsuccessful fracture healing, while the numerical simulations showed that optimal healing depends on the abilities of phagocytes to efficiently engulf debris. A variety of numerical simulations are also presented to monitor the healing of a broken bone under different biological conditions, suggesting multiple possible ways to guide clinical experiments and factors that can be manipulated to achieve optimal outcomes.

1   Introduction

Worldwide, more than 8.9 million fractures occur every year affecting 50% of women and 25% of men over the age of 50 (Loi et al., 2016; Pisani et al., 2016). Furthermore, 10–15% of these fractures either do not heal or take longer to heal (Gómez-Barrena et al., 2015). Also, the risk of impaired healing increases as the immune system functions weaken in patients of advanced age and with severe traumas (Gibon et al., 2017; Mangum et al., 2019; Recknagel et al., 2013). In addition, common clinical consequences of unsuccessfully healed fractures include prolonged hospitalization, rehabilitation, and disabilities, which result in high socioeconomic costs (Carlier et al., 2015; Loi et al., 2016). Immune cells, most importantly macrophages, have been identified as key regulators of the bone fracture repair process (Baht et al., 2018; Sinder et al., 2015). Reduced number of macrophages during the inflammatory response results in delayed union (Schlundt et al., 2018). However, systemic and high concentration of inflammatory cytokines delivered from the immune system restricts bone formation (Baht et al., 2018; Loi et al., 2016; Mangum et al., 2019; Schell et al., 2017). It has also been suggested that the deficiency in phagocytosis is a main contributing factor to unsuccessful healing (Elliott et al., 2017; Sinder et al., 2015). Yet, the role of the immune system cells in bone fracture healing has not been clearly understood (Baht et al., 2018; Pajarinen et al., 2019; Wu et al., 2013) and is an area of increasing interest not only in tissue regeneration but also in the treatment of autoimmune diseases (Elliott et al., 2017; Michalski et al., 2016; Sinder et al., 2015).

Mathematical models have been widely used in bone fracture healing to gain insights into the most fundamental aspects of bone formation (Ghiasi et al., 2017; Pivonka and Dunstan, 2012; Trejo and Kojouharov, 2019; Trejo et al., 2019a). Some of the first mathematical models that attempted to study the immune system involvements in the early stages of the bone fracture healing process were developed in Kojouharov et al. (2017) and Trejo et al. (2019b). In Kojouharov et al. (2017), a system of nonlinear ordinary differential equations was introduced to study the interactions among debris, macrophages, mesenchymal stem cells (MSCs), osteoblasts, pro- and anti-inflammatory cytokines, cartilage, and bone tissue. The mathematical findings revealed that the successful healing of a broken bone depends only on the bone cells' proliferation and differentiation rates. Further-

more, the numerical simulations revealed that high concentrations of pro-inflammatory cytokines negatively affect the healing time of a fracture while the administration of anti-inflammatory cytokines can accelerate it in a dose-dependent manner. The model in Kojouharov et al. (2017) was subsequently extended, in Trejo et al. (2019b), by incorporating the two distinct populations of macrophages: the classically activated macrophages and the alternatively activated macrophages. Even though the stability conditions obtained in Trejo et al. (2019b) for the long-term behavior of solutions were the same as in Kojouharov et al. (2017), the numerical simulations with the new model revealed the macrophages' importance in enhancing tissues production through their ability to deliver pro- and anti-inflammatory cytokines. The model also demonstrated that the success of treatments with anti-inflammatory cytokines depends heavily on debris densities. In addition, the numerical simulations showed that the macrophages' phagocytic rate drastically changes the short term tissues evolution. However, those mathematical models did not consider the important process of cellular migration due to pro-inflammatory cytokines (Baht et al., 2018; Marsell and Einhorn, 2011; Schmidt-Bleek et al., 2015) and also examined only specific phagocytic rates as functions of debris (M'Barek et al., 2015; Van Zon et al., 2009). In this paper, the models developed in Kojouharov et al. (2017) and Trejo et al. (2019b) are further modified to carefully study the effects of phagocytes and inflammatory cytokines on bone fracture healing during the inflammatory and repair phases of the process, which have an elapsed time occurring about 21 days after initial fracture (Einhorn and Gerstenfeld, 2015; Trejo et al., 2019b). The inhibitory effects of anti-inflammatory cytokines on pro-inflammatory cytokines production are incorporated by imposing maximal cellular densities and modeling cells migration to the injury site as proportional to the pro-inflammatory cytokines concentration up to a maximal constant rate. This approach directly accounts for the process of cellular migration being due to molecular factors (Arango Duque and Descoteaux, 2014; Italiani and Boraschi, 2014) rather than necrotic cells. The new model also explicitly incorporates the migration of MSCs during the early stage of bone fracture healing (Baht et al., 2018; Einhorn and Gerstenfeld, 2015; Marsell and Einhorn, 2011; Ullah et al., 2013). In addition, the engulfing rate is modeled with a generic function that depends on the debris concentration, which generalizes the properties of different mathematical phagocytic rate expressions proposed in the literature (Dunster et al., 2014; Gesztelyi et al., 2012; M'Barek et al., 2015; Reynolds et al., 2006; Trejo et al., 2019a,b).

The organization of the paper is as follows: Section 2 discusses the cellular and molecular interactions that occur during the bone fracture healing process. The simplifying assumptions are presented in Section 3, while the corresponding system of nonlinear ordinary differential equations is introduced in Section 4. The new model is theoretically analyzed in Section 5, where the stability, bifurcation, and sensitivity analyses of the system are presented. Numerically simulations that demonstrate the functionality of the model under different biological conditions are performed in Section 6. The paper concludes, in Section 7, with a discussion of mathematical and biological observations.

2   Biological Background

Bone fracture healing is a complex regenerative process which can be described in three characteristic phases: inflammatory, repair, and remodelling (Ghiasi et al., 2017; Pivonka and Dunstan, 2012). During the inflammatory phase, damaged tissue and necroses of cells deliver a variety of inflammatory mediators, such as the tumor necrosis factor-α (TNF-α) and interleukin-1 (IL-1), which activate and stimulate cellular migration toward the injury site (Marsell and Einhorn, 2011; Pajarinen et al., 2019). Local and migrating immune cells, including neutrophils, monocytes, and macrophages, control and resolve the inflammation by engulfing debris and down-regulating the inflammatory cytokines production (Italiani and Boraschi, 2014; Mountziaris and Mikos, 2008; Schmidt-Bleek et al., 2015). During the repair phase, resident and migrating MSCs proliferate and differentiate into fibroblasts, osteoblasts, and chondrocytes (Pajarinen et al., 2019). These cells proliferate and synthesize different types of collagen and proteins that in a process of mineralization result into fibrocartilage and woven bone (Bailon-Plaza and Van Der Meulen, 2001; Echeverri et al., 2015; Pajarinen et al., 2019). During the last phase, the two tissues are constantly removed and replaced by a functional bone (Einhorn and Gerstenfeld, 2015). This process is referred to as bone remodeling and consists of systematic tissue degradation and production by osteoclasts and osteoblasts, respectively (Marsell and Einhorn, 2011).

The different biological processes involved in bone fracture healing overlap and occur at different time scales (Gómez-Barrena et al., 2015). Under normal biological conditions, inflammation is usually resolved within the first two weeks of the healing process (Einhorn, 2005), as debris are eliminated, inflammatory cells emigrate to the lymphatic nods to die, and resident macrophages and inflammatory molecules return to their baseline concentrations (Marsell and Einhorn, 2011; Ricciotti and FitzGerald, 2011; Serhan and Savill, 2005). The repair phase starts around 3 days after injury, as fibrocartilage and woven bone are synthesized (Bailon-Plaza and Van Der Meulen, 2001). Finally, bone remodeling occurs, as osteoclasts populate the repair site and start removing the callus (Einhorn, 2005; Marsell and Einhorn, 2011). Bone remodeling is a slow process that can take months to years until the bone completely recovers to its pre-injury state (Einhorn and Gerstenfeld, 2015; Marsell and Einhorn, 2011). Conventionally, if a fracture is not healed after 4 months, it is considered a delayed union, while if the healing process has stopped completely within the first 6 months after the trauma without obtaining a functional bone, it is considered a nonunion (Gómez-Barrena et al., 2015; Pivonka and Dunstan, 2012). Specific radiological diagnoses are required to clearly distinguish between the two negative healing outcomes and in both cases either surgical interventions or drug administrations
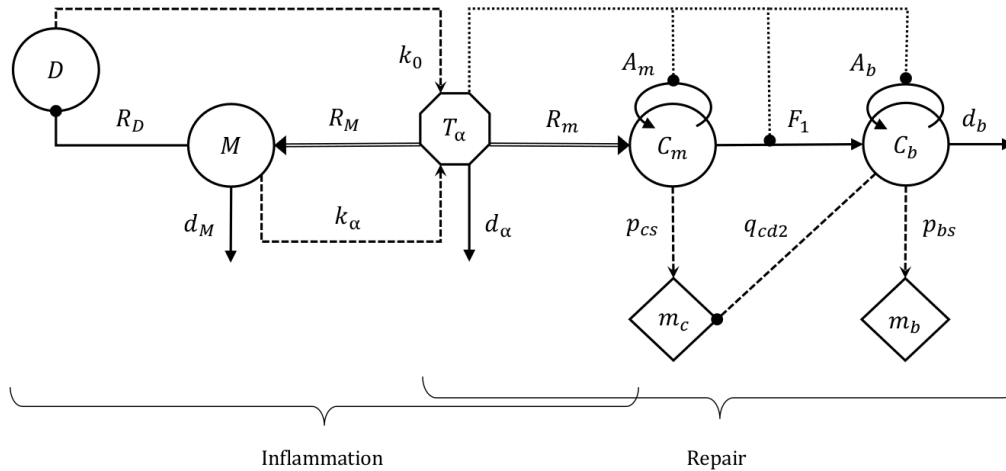
Figure 1: Flow diagram for the inflammatory and repair phases of the bone fracture healing process: Debris (D) and macrophages (M) release tumor necrosis factor-α (T_α), which is represented by dashed arrows. T_α activates the migration of M and MSCs (C_m), which is represented by compound arrows, inhibits cellular proliferation and differentiation (dotted-dot-ending arrows) and decays (solid arrows). M engulf debris and emigrate (solid-dot ending and solid arrows). C_m and osteoblasts (C_b) proliferate and differentiate (circular-solid and solid arrows). The cartilage (m_c) and the bone (m_b) are synthesized by C_m and C_b (dashed arrows), respectively. The m_c is degraded by the osteoclasts (dashed-dot-ending arrow), which are assumed to be proportional to C_b.

are needed in order to achieve successful repair (Bailon-Plaza and Van Der Meulen, 2001; Gómez-Barrena et al., 2015).

3   Modeling Assumptions

The most important effects of the phagocytes and inflammatory cytokines on bone fracture healing are observed during the inflammatory and repair phases of the healing process (Kojouharov et al., 2017; Schlundt et al., 2015; Trejo et al., 2019b). The healing process initiates with an acute inflammatory response characterized by immune cellular recruitment and the delivery of high concentrations of inflammatory mediators (Einhorn and Gerstenfeld, 2015; Trejo et al., 2019b). Then the modulation of inflammation and restoration of the homeostatic state occurs, as cellular migration, proliferation, differentiation and tissue production and degradation take place.

Modeling assumptions provide a way to simplify the complex processes involved in bone fracture healing, while preserving the important features of the system, which makes the resulting model both biologically realistic and mathematically tractable. In this paper, we consider debris (D), macrophages (M), MSCs (C_m), osteoblasts (C_b), TNF-α (T_α), fibrocartilage (m_c), and woven bone (m_b), as the primary variables during the inflammatory and repair phases of the healing process. Figure 1 illustrates the flow diagram for the two phases of the bone fracture healing process, where the cells and cellular dynamics are represented by the circular shapes and solid arrows. The cytokines (T_α) concentration and its production/decay are represented by the octagonal shape and dashed/solid arrows. T_α activation effects on the cellular recruitment are represented by the compound arrows, while its inhibitory effects on cellular proliferation and differentiation are represented by the dotted arrows. The tissues densities and their synthesis/degradation are represented by the rhomboidal shapes and dashed arrows. Removal of debris and the negative effects among the variables are represented by the dot-ending arrows.

The healing process initiates with the delivery of pro-inflammatory cytokines, modeled with T_α, and being produced by D (Einhorn and Gerstenfeld, 2015), where the density of D is in proportion to the necrotic cellular density (Kojouharov et al., 2017) resulting after the trauma. Then T_α stimulates the migration and activation of macrophages and MSCs toward the healing site (Baht et al., 2018; Einhorn and Gerstenfeld, 2015; Marsell and Einhorn, 2011). The migration rates are modeled proportional to T_α up to maximal constant rates, k_M and k_m, (Newman et al., 1982; Ullah et al., 2013) imposed by the inhibitory effects of anti-inflammatory cytokines (Italiani and Boraschi, 2014; Kojouharov et al., 2017; Trejo et al., 2019b). Macrophages engulf debris and release T_α in response to their phagocytic activities (Italiani and Boraschi, 2014; Trejo et al., 2019b). MSCs proliferate and differentiate toward fibroblasts, chondrocytes, and osteoblasts which also proliferate and differentiate into osteocytes (Bailon-

Table 1: Model variables and parameters.

Variable/Parameter	Description	Units
D	Debris	cells/mL
M	Macrophages	cells/mL
C_m	MSCs	cells/mL
C_b	Osteoblasts	cells/mL
T_α	TNF-α	ng/mL
m_c	Fibrocartilage	g/mL
m_b	Woven bone	g/mL
k_d	Macrophages phagocytic rate	1/day
a_{ed}	Half-saturation of debris	cells/mL
K_{lM}	Maximal macrophages density	cells/mL
k_M	Migration rate of M	cells/ng/day
d_M	Emigration rate of M	1/day
k_m	Migration rate of C_m	cells/ng/day
k_0	Secretion rate of T_α by D	ng/cells/day
k_α	Secretion rate of T_α by M macrophages	ng/cells/day
d_α	Decay rate of T_α	1/day
a_{pm}	Effectiveness of T_α inhibition of C_m proliferation	ng/mL
a_{mb}	Effectiveness of T_α inhibition of C_m differentiation	ng/mL
a_{pb}	Effectiveness of T_α inhibition of C_b proliferation	ng/mL
a_{pm_1}	Constant enhancement of T_α to C_m proliferation	ng/mL
k_{pm}	Proliferation rate of C_m	1/day
d_m	Maximal differentiation rate of C_m to C_b	1/day
k_{pb}	Proliferation rate of C_b	1/day
d_b	Differentiation rate of C_b	1/day
p_{cs}	Fibrocartilage synthesis rate	g/cells/day
q_{cd_1}	Fibrocartilage degradation rate	mL/cells/day
q_{cd_2}	Fibrocartilage degradation rate by osteoclasts	mL/cells/day
p_{bs}	Bone tissue synthesis rate	g/cells/day
q_{bd}	Bone tissue degradation rate	mL/cells/day
K_{lb}	Carrying capacity of C_b	cells/mL
K_{lm}	Carrying capacity of C_m	cells/mL

Plaza and Van Der Meulen, 2001). Fibroblast and chondrocyte densities are assumed to be in proportion to C_m density (Trejo et al., 2019b). Therefore, C_m and C_b synthesize m_c and m_b, respectively (Bailon-Plaza and Van Der Meulen, 2001; Trejo et al., 2019b), where m_c is constantly removed by the osteoclasts, with the density of the osteoclasts being assumed proportional to the density of the osteoblasts (Bailon-Plaza and Van Der Meulen, 2001).

In addition, both cellular migration and proliferation rates decrease linearly as the populations' sizes approach a maximum value, K_{lM}, K_{lm}, and K_{lb}, forced by the limited resources of the environment and the anti-inflammatory cytokines regulatory effects (Arango Duque and Descoteaux, 2014; Bailon-Plaza and Van Der Meulen, 2001; Newman et al., 1982; Trejo et al., 2019b; Ullah et al., 2013). T_α also inhibit both C_b proliferation and C_m differentiation (Kojouharov et al., 2017; Trejo et al., 2019b). However, low concentration levels of T_α increase C_m proliferation (Bastidas-Coral et al., 2016) while high levels of T_α restrict C_m proliferation (Trejo et al., 2019b). Furthermore, it is assumed that M increase in size only due to recruitment (Trejo et al., 2019b), as there is no evidence that they proliferate during the healing of a broken bone (Swirski et al., 2014), and they emigrate at a constant rate, d_M, to the lymphatic nods to die (Serhan and Savill, 2005). There is no recruitment of osteoblasts (Ullah et al., 2013; Bailon-Plaza and Van Der Meulen, 2001) and they remain at the healing site to continue with the remodeling phase of the healing process (Bailon-Plaza and Van Der Meulen, 2001). Bone fracture healing is governed by the production of m_c and m_b (Bailon-Plaza and Van Der Meulen, 2001; Carlier et al., 2015), whose final levels are used to classify the healing outcome as delayed or nonunion healing (Trejo et al., 2019b).

4　Mathematical Model

The inflammation and repair phases of the bone fracture healing process are modeled with a mass-action system of nonlinear ordinary differential equations, where all variables represent homogeneous quantities in a given volume. The model variables and parameters, including their corresponding units, are described in Table 1. Following the flow diagram given in Figure 1 and the modeling assumptions provided in Section 3 yields the resulting system of equations:

$$\frac{dD}{dt} = \underbrace{-R_D M}_{\text{clearance of debris}} \tag{1}$$

$$\frac{dM}{dt} = \underbrace{R_M}_{\text{migration}} - \underbrace{d_M M}_{\text{emigration}} \tag{2}$$

$$\frac{dT_\alpha}{dt} = \underbrace{k_0 D + k_\alpha M}_{\text{production}} - \underbrace{d_\alpha T_\alpha}_{\text{degradation}} \tag{3}$$

$$\frac{dC_m}{dt} = \underbrace{R_m}_{\text{migration}} + \underbrace{A_m C_m \left(1 - \frac{C_m}{K_{lm}}\right)}_{\text{proliferation}} - \underbrace{F_1 C_m}_{\substack{\text{osteogenic} \\ \text{differentiation}}} \tag{4}$$

$$\frac{dC_b}{dt} = \underbrace{A_b C_b \left(1 - \frac{C_b}{K_{lb}}\right)}_{\text{proliferation}} + \underbrace{F_1 C_m}_{\substack{\text{osteogenic} \\ \text{differentiation}}} - \underbrace{d_b C_b}_{\substack{\text{osteocytic} \\ \text{differentiation}}} \tag{5}$$

$$\frac{dm_c}{dt} = \underbrace{(p_{cs} - q_{cd_1} m_c) C_m}_{\text{production}} - \underbrace{q_{cd_2} m_c C_b}_{\text{degradation}} \tag{6}$$

$$\frac{dm_b}{dt} = \underbrace{(p_{bs} - q_{bd} m_b) C_b}_{\text{production}}. \tag{7}$$

Equation (1) describes the rate of change with respect to time of the debris density. It decreases proportionally to M, where the phagocytic rate, $R_D = R_D(D)$, is a function of the debris with the following properties (Gesztelyi et al., 2012):

- $R_D(x) > 0$ for all $x > 0$, with $R_D(0) = 0$; and

- $R_D(x)$ is a continuously differentiable function in $[0, \infty)$, with $R'_D(0) \geq 0$.

Examples of such functions that have been widely used in various mathematical models include (Dunster et al., 2014; Gesztelyi et al., 2012; M'Barek et al., 2015; Reynolds et al., 2006; Torres et al., 2019; Trejo et al., 2019b):

$$R_D = \frac{k_d}{a_{ed}} D, \tag{8}$$

and

$$R_D = \frac{k_d D^n}{a_{ed}^n + D^n}, \quad n \geq 1. \tag{9}$$

In Equation (8), the engulfment rate increases proportional to debris density while in Equation (9) the phagocytic rate saturates for D large (Gesztelyi et al., 2012). Furthermore, the function provided in Equation (8) is written in a form that represents a linear approximation of the function R_D given in Equation (9) when $n = 1$. We use the general form of the function $R_D(x)$ in the model analysis presented below, while we implement the specific forms given in Equations (8) and (9) with $n = 1, 2$ in the numerical simulations as they have been widely used in other mathematical models (Dunster et al., 2014; Torres et al., 2019; Trejo et al., 2019b).

Equation (2) describes the rate of change with respect to time of macrophages density. It increases because of migration and decreases at a constant emigration rate. It is assumed that M migrate to the injury site proportionally to T_α up to a maximal

constant rate, k_M (Arango Duque and Descoteaux, 2014; Dunster et al., 2014; Italiani and Boraschi, 2014):

$$R_M = k_M \left(1 - \frac{M}{K_{lM}}\right) T_\alpha.$$

Equation (3) describes the rate of change with respect to time of T_α, which increases due to D and M productions, and decreases by degradation. Equation (4) describes the rate of change with respect to time of C_m. It increases by cellular migration and division up to a constant-maximal carrying capacity, K_{lm}, and decreases by differentiation (Bailon-Plaza and Van Der Meulen, 2001). The migration rate of C_m is modeled to be proportional to T_α up to K_{lm} (Ullah et al., 2013):

$$R_m = k_m \left(1 - \frac{C_m}{K_{lm}}\right) T_\alpha.$$

The total MSCs proliferation rate is modeled by (Kojouharov et al., 2017; Sherratt and Murray, 1990; Trejo et al., 2019b):

$$A_m = k_{pm} \times \frac{a_{pm}^2 + a_{pm_1} T_\alpha}{a_{pm}^2 + T_\alpha^2},$$

where in the absence of inflammation, $T_\alpha = 0$, C_m proliferate at a constant rate k_{pm}. However, when there is inflammation, $T_\alpha > 0$, the proliferation rate of C_m increases or decreases according to the concentration of T_α, i.e., high concentration levels of T_α inhibit C_m proliferation while low concentration levels of T_α accelerate C_m proliferation (Bastidas-Coral et al., 2016). The differentiation rate of C_m is inhibited by T_α, which is modeled by the following function (Kojouharov et al., 2017; Trejo et al., 2019b):

$$F_1 = d_m \times \frac{a_{mb}}{a_{mb} + T_\alpha}.$$

Equation (5) describes the rate of change with respect to time of C_b. It increases when C_m differentiate into osteoblasts or when osteoblasts proliferate (Bailon-Plaza and Van Der Meulen, 2001). It decreases at a constant rate d_b when osteoblasts differentiate. The osteoblasts proliferation rate is inhibited by T_α, which is modeled by the following function (Kojouharov et al., 2017; Trejo et al., 2019b):

$$A_b = k_{pb} \times \frac{a_{pb}}{a_{pb} + T_\alpha}.$$

Equations (6) and (7) describe the rate of change with respect to time of the fibrocartilage and woven bone, respectively, where p_{cs} and p_{bs} are the tissue constant production rates and q_{cd1}, q_{cd2}, and q_{bd} are the tissue degradation rates (Bailon-Plaza and Van Der Meulen, 2001; Trejo et al., 2019b).

5 Model Analysis

The analysis of Model (1)–(7) is done by first performing the stability analysis of the system, where the equilibria of the system and their corresponding stability properties are studied mathematically. Each equilibrium provides a possible outcome of the bone fracture healing process and its corresponding stability properties define the conditions under which a particular healing result occurs. Next, a bifurcation analysis on the equilibria is provided to support their properties and dependency on model parameters. Finally, sensitivity analysis of the model is presented to identify the most influential parameters in the variability of the bone fracture healing outcomes.

5.1 Stability analysis

Note that System (1)–(7) is well-posed and that all solutions remain within the state space, $D \geq 0$, $M \geq 0$, $T_\alpha \geq 0$, $C_m \geq 0$, $C_b \geq 0$, $m_c \geq 0$ and $m_b \geq 0$, since the right-hand side functions of System (1)–(7) are continuously differentiable and bounded (Stuart and Humphries, 1998). The analysis of Model (1)–(7) is done by finding the equilibria, denoted by $E_i(D, M, T_\alpha, C_m, C_b, m_c, m_b)$, $i = 0, 1, 2, 3$, and their corresponding stability properties. Setting the right-hand sides of the equations (1)–(7) equal to zero yields the following four equilibria:

$$E_0(0, 0, 0, 0, 0, m_{c_0}^*, m_{b_0}^*), \qquad E_1(0, 0, 0, 0, K_{lb}(1 - d_b/k_{pb}), 0, p_{bs}/q_{bd}),$$

$$E_2(0, 0, 0, K_{lm}(1 - d_m/k_{pm}), C_{b_2}^*, m_{c_2}^*, p_{bs}/q_{bd}), \qquad E_3(0, M^*, T_\alpha^*, C_{m_3}^*, C_{b_3}^*, m_{c_3}^*, p_{bs}/q_{bd}).$$

The biological meanings of the above equilibria are summarized in Table 2. The steady-state E_0 represents an unsuccessful healing outcome. In this case, the inflammation is been resolved since debris, macrophages, and TNF-α densities are zero but

Table 2: Biological meanings of the equilibria.

Equilibria	Biological meanings
E_0	nonunion with resolved inflammatory response
E_1	successful healing
E_2	delayed or nonunion healing with resolved inflammatory response
E_3	delayed or nonunion healing with chronic inflammation response

Table 3: Existence and local stability conditions of the equilibrium points.

Equilibria	Existence	Stability
E_0	$m_{c_0}^*, m_{b_0}^* \geq 0$	$k_\alpha k_M < d_\alpha d_M, k_{pm} \leq d_m, k_{pb} \leq d_b$
E_1	$k_{pb} > d_b$	$k_\alpha k_M < d_\alpha d_M, d_m \geq k_{pm}$
E_2	$k_{pm} > d_m$	$k_\alpha k_M < d_\alpha d_M$
E_3	$k_\alpha k_M > d_\alpha d_M$	always

the repair process has failed since the osteoblasts and osteoclasts have died out before the beginning of the remodeling process. Hence, the tissue densities, $m_{c_0}^*$ and $m_{b_0}^*$, can be any two positive values smaller or equal than their maximal densities, p_{cs}/q_{cd1} and p_{bs}/q_{bd}, respectively (see Theorem 1). The steady-state E_1 represents a successful repair of the bone fracture, where the inflammation is resolved, the fibrocartilage is completely removed, and the woven bone has achieved its maximal density. The steady-state E_2 represents a nonunion or delayed union, where the inflammation is resolved but the osteoclasts have failed to degrade the cartilage in a timely fashion. The steady-state E_3 represents a nonunion or delayed union with a chronic inflammation, since even though debris are completely removed, $D = 0$, the macrophages and the TNF-α remain at the healing site and the osteoclasts have failed to degrade the fibrocartilage.

Table 3 summarizes the equilibria and their corresponding existence and stability conditions. The existence conditions of each equilibrium point arise from the fact that all biologically meaningful variables are non-negative. E_0 exists for all non-negative steady state tissue densities, i.e., $m_{c_0}^*, m_{b_0}^* \geq 0$. E_1 exists when osteoblasts proliferate faster than they differentiate, i.e., $k_{pb} > d_b$. E_2 exists when the MSCs proliferation rate is bigger than their differentiation rate, i.e., $k_{pm} > d_m$. E_3 exists when the influx rates of macrophages and TNF-α are more than their outflux rates, i.e., $k_\alpha k_M > d_\alpha d_M$. Similar biological interpretations of the stability conditions can be made for each equilibrium point.

The stability of the equilibria is analyzed using the Jacobian of System (1)–(7) at each equilibrium point and finding its corresponding eigenvalues (Otto and Day, 2011). The following theorems hold for the general form of the phagocytic rate function $R_D(x)$ given above, and, in particular, for the specific forms given in Equations (8) and (9):

Theorem 1. *Suppose that $m_{c_0}^* \geq 0$ and $m_{b_0}^* \geq 0$. Then $E_0(0, 0, 0, 0, 0, m_{c_0}^*, m_{b_0}^*)$ exists for all the parameter values and E_0 belongs to the set $B = \{(0, 0, 0, 0, 0, m_c, m_b) : 0 \leq m_c \leq p_{cs}/q_{cd1}, 0 \leq m_b \leq p_{bs}/q_{bd}\}$, which is a local attractor set of the solution set given by System (1)–(7) if and only if $k_M k_\alpha < d_\alpha d_M, k_{pm} \leq d_m$, and $k_{pb} \leq d_b$.*

Proof. The elements of E_0 are non-negative for all parameter values of the model, hence E_0 is a biologically feasible equilibrium. Next, it will be proved that the hyperplane $A = \{(0, 0, 0, 0, 0, m_c, m_b) : m_c \geq 0, m_b \geq 0\}$ is an attractor set of the solutions of System (1)–(7). There are two cases to consider based on the relation between the cells proliferation and differentiation rates. First, let us examine the case when $k_{pm} < d_m$ and $k_{pb} < d_b$. The Jacobian matrix $J(E_0)$ is given by the following lower triangular block matrix:

$$J(E_0) = \begin{pmatrix} J_1(E_0) & \mathbf{0} & \mathbf{0} \\ J_1^* & J_2(E_0) & \mathbf{0} \\ \mathbf{0} & J_2^* & J_3(E_0) \end{pmatrix},$$

where

$$J_1(E_0) = \begin{pmatrix} 0 & 0 & 0 \\ 0 & -d_M & k_M \\ k_0 & k_\alpha & -d_\alpha \end{pmatrix}, \qquad J_2(E_0) = \begin{pmatrix} -d_m + k_{pm} & 0 \\ d_m & -d_b + k_{pb} \end{pmatrix}, \qquad J_3(E_0) = \begin{pmatrix} 0 & 0 \\ 0 & 0 \end{pmatrix},$$

and J_1^*, J_2^* are non-zero submatrices. Therefore, the corresponding characteristic polynomial associated with $J(E_0)$ is given by the product of the characteristic polynomials associated with each submatrix (Strang et al., 1993):

$$p(\lambda) = \lambda^3 \left(\lambda^2 + (d_M + d_\alpha)\lambda + d_M d_\alpha - k_M k_\alpha\right) \left(\lambda + d_m - k_{pm}\right) \left(\lambda + d_b - k_{pb}\right).$$

Hence, from Routh-Hurwitz criteria, $n = 2$, the eigenvalues of $J(E_0)$ are negative or have negative real part, for the variables M, T_α, C_m, and C_b, and are equal to zero, for D, m_c, and m_b. Since $D'(t) \leq 0$ for all the variables in the system (1)–(7) and $(D^*, 0, 0, 0, 0, m_c, m_b)$ with $D^* \neq 0$ is not an equilibrium point, then the solutions of the system (1)–(7) are attracted to the set $A = \{(0, 0, 0, 0, 0, m_c, m_b) : m_c \geq 0, m_b \geq 0\}$. Equations (6) and (7) imply that $m_c' \leq 0$ and $m_b' \leq 0$ for all $m_c > p_{cs}/q_{cd_1}$ and $m_b > p_{bs}/q_{bd}$. Therefore, the set B is a local attractor set of A (Stuart and Humphries, 1998).

Next, let us consider the case when $k_{pm} = d_m$ and $d_b = k_{pb}$. Here, the eigenvalues of $J(E_0)$ are the same as above except those associated with C_m and C_b, which are equal to zero. Therefore, in this case, considering the second order approximations of the right hand sides of Equations (4) and (5), instead of just the first order approximations, and using similar arguments as above, proves that the set B is a local attractor set of A. $\qquad\square$

Theorem 2. *The equilibrium $E_1(0, 0, 0, 0, K_{lb}(1 - d_b/k_{pb}), 0, p_{bs}/q_{bd})$ exists when $k_{pb} > d_b$, and it is locally stable if and only if $k_\alpha k_M < d_\alpha d_M$ and $d_m \geq k_{pm}$.*

Proof. E_1 is a biologically feasible equilibrium, since all the elements of E_1 are non-negative for all parameter values of the model, with $k_{pb} > d_b$. Next, the Jacobian matrix corresponding to E_1 is given by the following lower triangular block matrix:

$$J(E_1) = \begin{pmatrix} J_1(E_1) & \mathbf{0} & \mathbf{0} \\ J_1^* & J_2(E_1) & \mathbf{0} \\ \mathbf{0} & J_2^* & J_3(E_1) \end{pmatrix},$$

where $J_1(E_1)$ has the same expression as $J_1(E_0)$, defined in Theorem 1, J_1^* and J_2^* are nonzero sub-matrices and

$$J_2(E_1) = \begin{pmatrix} -d_m + k_{pm} & 0 \\ d_m & d_b - k_{pb} \end{pmatrix}, \qquad J_3(E_1) = \begin{pmatrix} -q_{cd_2}K_{lb}(1 - \frac{d_b}{k_{pb}}) & 0 \\ 0 & -q_{bd}K_{lb}(1 - \frac{d_b}{k_{pb}}) \end{pmatrix}.$$

Since $d_m \geq k_{pm}$ and $k_{pb} > d_b$ and all the eigenvalues of $J_1(E_0)$ are non-positive values, then all the eigenvalues of $J(E_1)$ are all negative except the eigenvalues associated with D and C_m, when $k_{pm} = d_m$, which are equal to zero. Therefore, by applying similar arguments provided in the proof of Theorem 1 when the eigenvalues are zero, it implies that E_1 is a locally stable node. $\quad\square$

Theorem 3. *The equilibrium $E_2(0, 0, 0, C_m^*, C_b^*, m_c^*, p_{bs}/q_{bd})$, where $C_m^* = K_{lm}(1 - d_m/k_{pm})$, $m_c^* = p_{cs}C_m^*/(q_{cd_1}C_m^* + q_{cd_2}C_b^*)$, $C_b^* = K_{lb}(k_{pb} - d_b + \sqrt{(k_{pb} - d_b)^2 + 4k_{pb}d_mC_m^*/K_{lb}})/2k_{pb}$, exists when $k_{pm} > d_m$ and it is locally stable if and only if $k_M k_\alpha < d_\alpha d_M$.*

Proof. From the definition of E_2, the elements of E_2 are nonnegative for all parameter values of the model with $k_{pm} > d_m$. Hence, E_2 is a biologically feasible equilibrium. Next, the Jacobian matrix corresponding to E_2 is given by the following lower triangular block matrix:

$$J(E_2) = \begin{pmatrix} J_1(E_2) & \mathbf{0} & \mathbf{0} \\ J_1^* & J_2(E_2) & \mathbf{0} \\ \mathbf{0} & J_2^* & J_3(E_2) \end{pmatrix},$$

where $J_1(E_2)$ has the same expression as $J_1(E_0)$, defined in Theorem 1, J_1^* and J_2^* are nonzero submatrices, and

$$J_2(E_2) = \begin{pmatrix} d_m - k_{pm} & 0 \\ d_m & -\sqrt{(d_b - k_{pb})^2 + 4k_{pb}d_mC_m^*/K_{lb}} \end{pmatrix}, \qquad J_3(E_2) = \begin{pmatrix} -q_{cd_1}C_m^* - q_{cd_2}C_b^* & 0 \\ 0 & -q_{bd}C_b^* \end{pmatrix}.$$

Since $k_{pm} > d_m$, and all equilibrium variables and parameter values are positive, then all the eigenvalues of $J_1(E_2), J_2(E_2), J_3(E_2)$ are negative except for the eigenvalue associated to D which is equal to zero. Following the same arguments applied in the proof of Theorem 1 for the eigenvalue that equals to zero, it can be concluded that E_2 is locally stable. $\quad\square$

Theorem 4. *The equilibrium $E_3(0, M^*, T_\alpha^*, C_m^*, C_b^*, m_c^*, p_{bs}/q_{bd})$, where $M^* = K_{lM}(1 - d_M d_\alpha/k_M k_\alpha)$, $T_\alpha^* = k_\alpha M^*/d_\alpha$, $C_b^* = K_{lb}(A_b^* - d_b + \sqrt{(A_b^* - d_b)^2 + 4A_b^* F_1^* C_m^*/K_{lb}})/2A_b^*$, $C_m^* = K_{lm}(A_m^* - F_1^* - R_m^*/K_{lm} + \sqrt{(A_m^* - F_1^* - R_m^*/K_{lm})^2 + 4A_m^* R_m^*/K_{lm}})/2A_m^*$, exists when $k_\alpha k_M > d_\alpha d_M$ and it is locally stable. Here, A_m^*, A_b^*, F_1^*, and R_m^* represent the values of each corresponding rate at T_α^*, and m_c^* has the same expression as in Theorem 3.*

Proof. From the definition of E_3, the elements of E_3 are nonnegative for all parameter values of the model. Hence, E_3 is a biologically feasible equilibrium. Next, the Jacobian matrix corresponding to E_3 is given by the following lower triangular block matrix:

$$J(E_3) = \begin{pmatrix} J_1(E_3) & \mathbf{0} & \mathbf{0} \\ J_1^* & J_2(E_3) & \mathbf{0} \\ \mathbf{0} & J_2^* & J_3(E_3) \end{pmatrix},$$
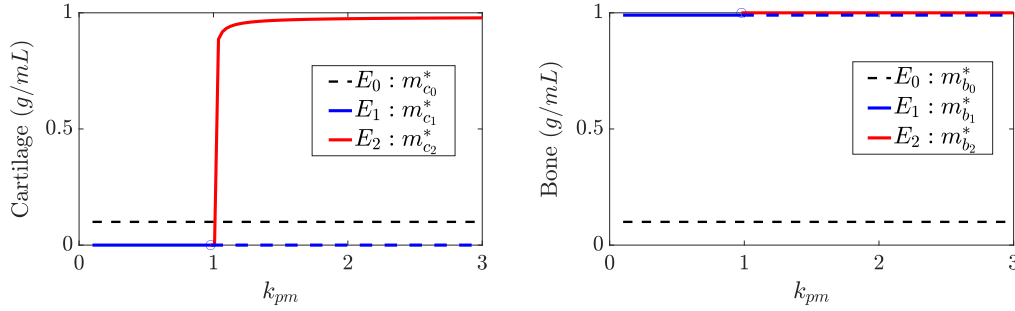
Figure 2: Bifurcation diagram of System (1)–(7) for the steady state cartilage (m_c^*) and bone (m_b^*) variables, as k_{pm} is varied from 0.1 to 3: solid lines represent stable states while dashed lines represent unstable states. E_0 and E_1 exist for all k_{pm} values while E_2 exists when $k_{pm} > 1 = d_m$. E_1 changes stability at $k_{pm} = 1$ while E_2 does not exist for values of k_{pm} below 1.

where $J_3(E_3)$ has similar expression as $J_3(E_2)$ defined in Theorem 3, J_1^* and J_2^* are nonzero submatrices, and

$$J_1(E_3) = \begin{pmatrix} -M^* R_D'(0) & 0 & 0 \\ 0 & -k_M k_\alpha/d_\alpha & d_M d_\alpha/k_\alpha \\ k_0 & k_\alpha & -d_\alpha \end{pmatrix}, \qquad J_2(E_3) = \begin{pmatrix} -j_1 & 0 \\ F_1^* & -j_2 \end{pmatrix},$$

where

$$j_1 = \sqrt{(A_m^* - F_1^* - R_m^*/K_{lm})^2 + 4A_m^* R_m^*/K_{lm}} \quad \text{and} \quad j_2 = \sqrt{(A_b^* - d_b)^2 + 4A_b^* F_1^* C_m^*/K_{lb}}.$$

From these submatrices, it is easy to prove that all the eigenvalues of $J(E_3)$ are negative except for the eigenvalue associated with D which is equal to zero when $R_D'(0) = 0$. If this is the case, then following the same arguments applied in the proof of Theorem 1 for the eigenvalue that equals to zero, it can be concluded that E_3 is locally stable. □

5.2 Bifurcation Analysis

The stability analysis revealed the dependence of the long-term dynamics of System (1)–(7) on its parameter values. Here, we further study numerically the behavior of the system by looking at the bifurcation of each equilibrium point with respect to specific key parameters, such as k_{pm} and k_M, which are varied in the biologically meaningful interval $(0, \infty)$, while fixing all other model parameter values (Wiggins, 2003). Our goal is to understand the effects of perturbing the values of these two parameters on the number and position of the steady states, which correspond to successful healing and delayed or nonunion healing with and without chronic inflammation responses.

Let us consider the case of resolved inflammation, i.e., $k_\alpha k_M < d_\alpha d_M$, and the case of chronic inflammation, i.e., $k_\alpha k_M > d_\alpha d_M$. In the first case, the proliferation rate of C_m, k_{pm}, is varied from 0.1 to 3 (1/day) and in the second case the migration rate of M, k_M, is varied from 1 to 8×10^5 (cells/ng/day). The rest of the system parameters are set to their baseline values (Table 1). In the figures below, the steady state variables m_c^* and m_b^* of each equilibrium point are plotted, when they exist, while the other steady state variables are omitted, since their qualitative behaviour is similar to the qualitative behaviour of the plotted steady state variables. In addition, the steady state variables $m_{c_0}^*$ and $m_{b_0}^*$ for E_0 are set to 0.1 (g/mL) as a representative example (Theorem 1). Under these conditions, E_1, the successful healing outcome, is always observed but its stability properties change when perturbing the parameters (Theorem 2). In all the figures, we refer to fibrocartilage, m_c, and woven bone, m_b, as cartilage and bone, respectively.

Figure 2 shows the bifurcation diagrams for the steady state of the variables m_c^* and m_b^* for the equilibria E_0 (black lines), E_1 (blue lines) and E_2 (red lines) in the case when $k_\alpha k_M < d_\alpha d_M$ and k_{pm} is varied (solid lines represent stable states while dashed lines represent unstable states). In addition, in this case, E_3 does not exist (Theorem 4), as $k_\alpha k_M = 0.415 < d_\alpha d_M = 1.5476$. The bifurcation occurs at $k_{pm} = 1$, where the stability of E_1 changes: it is stable when $k_{pm} \leq 1 = d_m$ and it is unstable otherwise. While E_2 exits only when $k_{pm} > d_m = 1$. E_0 always exits but it is unstable in the entire interval. The figure suggests that if the proliferation rate of C_m is greater than the C_m differentiation rate ($k_{pm} > 1 = d_m$) then E_2 is observed. In this case, MSCs and osteoblasts remain at the healing site, $C_{m_2}^*, C_{b_2}^* > 0$, where also fibroblasts, chondrocytes, and osteoclasts are present, and they constantly synthesize and degrade the fibrocartilage, $m_{c_2}^*$, and the woven bone $m_{b_2}^*$, respectively. However, the healing process results in a delayed or nonunion healing when the inflammation is resolved, $D^*, M^*, T_\alpha^* = 0$, but the fibrocartilage is not completely removed, $m_{c_2}^* > 0$, from the repair site.

Figure 3 shows the bifurcation diagrams for the steady state of the variables m_c^* and m_b^* for the equilibria E_0 (black lines), E_1 (blue lines) and E_3 (red lines) in the case when k_M is varied (solid lines represent stable states while dashed lines represent unstable
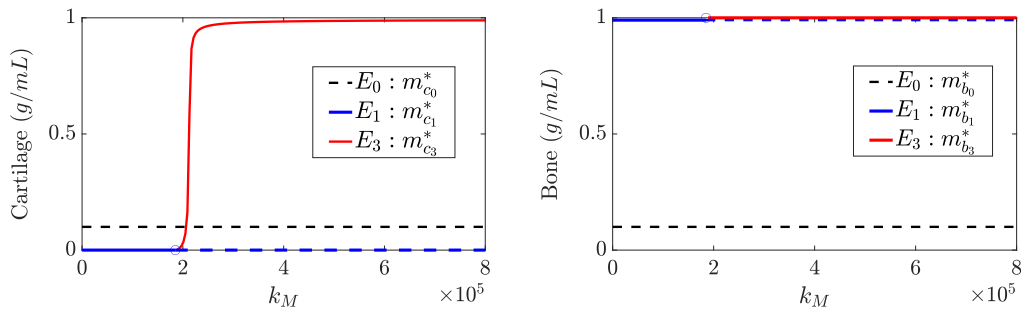
Figure 3: Bifurcation diagram of System (1)–(7) for the steady state cartilage (m_c^*) and bone (m_b^*) variables, as k_M is varied between 1 to 8×10^5: solid lines represent stable states while dashed lines represent unstable states. E_0 and E_1 exists for all k_M values while E_3 exists when $k_M > d_\alpha d_M/k_\alpha = 1.9 \times 10^5$. E_1 changes stability at $k_M = 1.9 \times 10^5$, while E_3 does not exit for values of k_M below 1.9×10^5.

states). In this case E_2 does not exist (Theorem 3), as $k_{pm} = 0.5 < d_m = 1$. The bifurcation occurs at $k_M = 1.9 \times 10^5$. Since E_1 is stable for values of k_M below 1.9×10^5 and unstable for values above it, while E_3 only exits when $k_M > 1.9 \times 10^5 = d_\alpha d_M/k_\alpha$. E_0 always exits but it is unstable in the entire interval. The figure suggests that increasing the migration rate the of macrophages, k_M, in a moderate fracture, above 1.9×10^5, the healing process will result in a delayed or nonunion healing with a chronic inflammation stage, since in this case E_3 is stable. Similarly as in the previous case, the MSCs and osteoblasts remain at the healing site, $C_{m_3}^*, C_{b_3}^* > 0$, and they constantly synthesize and degrade fibrocartilage, $m_{c_3}^*$, and woven bone $m_{b_3}^*$. However, the inflammation is not resolved as $M_3^* > 0$, $T_{\alpha_3}^* > 0$, and osteoclasts fail to remove the fibrocartilage, $m_{c_3}^* > 0$.

5.3   Sensitivity Analysis

Global sensitivity analysis is performed to identify the most influential parameters of Model (1)–(7) in the variability of the bone fracture healing outcomes. The eFAST (Extended Fourier Amplitude Sensitivity Test) method is implemented for the parameter sensitivity analysis, since it is one of the most reliable techniques among the variance-based methods that return the percentage variance of the model outputs given a set of parameters values (Marino et al., 2008). In eFAST, all parameters are varied within specific ranges at the same time and the sensitivity indices are calculated. The magnitude of the resulting sensitivity indices determines the importance of the parameters on the model variability outcomes (Marino et al., 2008; Saltelli et al., 1999).

To perform the parameter sensitivity analysis, three specific phagocytic rates are used: Equation (8), Equation (9) with $n = 1$, and Equation (9) with $n = 2$, which are denoted by R_{D0}, R_{D1}, and R_{D2}, respectively. All parameters are varied accordingly to the specific ranges and baseline values defined in Table 4, assuming that they follow uniform distributions. The initial condition for debris is set to $D(0) = 5 \times 10^7$ and the rest of the initial conditions are set to zero. The sensitivity indices for each model variable are calculated at day 21, which corresponds to the elapsed time for the inflammatory and repair phases of the bone fracture healing process (Einhorn and Gerstenfeld, 2015; Trejo et al., 2019b). Here, we only present and discuss the sensitivity results for the fibrocartilage and the woven bone densities, m_c and m_b, as these two quantities are used to classify the different bone fracture healing outcomes (Trejo et al., 2019b).

Figure 4 shows the individual contribution of each model parameter to the variance of each tissue density under the effect of each phagocytic rate: R_{Di}, $i = 0, 1, 2$. As it can be seen in the figure, for all phagocytic rates, R_{D0}, R_{D1}, and R_{D2}, the most influential parameters to the variability of the model outputs are the rates of cartilage production and degradation by osteoclasts, p_{cs}, q_{cd2}, and the bone tissue degradation rate p_{bs}. The rates p_{cs} and q_{cd2} account for more than 20% of the total cartilage density variance per each parameter, while p_{bs} accounts for more than 50% of the total bone tissue variance, for all phagocytic rates.

6   Numerical Simulations

In this section, Model (1)–(7) is used to investigate the progression of the healing of a broken bone under different biological conditions. Table 4 summarizes the parameter values used in the numerical simulations, which have been estimated in a qualitative manner from available data in other studies. All values are based on murine experiments, but can easily be adjusted to represent the bone fracture healing process in humans (Gibon et al., 2017; Marsell and Einhorn, 2011; Pivonka and Dunstan, 2012). The baseline parameter values represent healthy mice having a moderate fracture, i.e., a broken bone with a gap size less than 3 mm (Bailon-Plaza and Van Der Meulen, 2001; Isaksson, 2012). These baseline values also satisfy the stability conditions to observe a successful bone healing.

Table 4: Parameter values used in simulations.

| Parameter	Range	Baseline Value	Units	Reference
k_d	$[3, 48]$	13	1/day	Marée et al., 2005; Nagaraja et al., 2014
a_{ed}	$[4.71 \times 10^6, 5 \times 10^6]$	4.71×10^6	cells/mL	Nagaraja et al., 2014; Newman et al., 1982
K_{lM}	$[6 \times 10^5, 1 \times 10^6]$	1×10^6	cells/mL	Newman et al., 1982; Van Furth et al., 1973
k_M	$[5 \times 10^4, 7 \times 10^5]$	5×10^4	cells/ng/day	Van Furth et al., 1973
d_M	$[0.121, 0.2]$	0.121	1/day	Wang et al., 2012; Yu, 2014
k_m	$[1 \times 10^3, 3.4 \times 10^4]$	1×10^3	cells/ng/day	Ullah et al., 2013
k_0	$[2 \times 10^{-8}, 8.5 \times 10^{-6}]$	8.5×10^{-6}	ng/cells/day	Kojouharov et al., 2017; Nagaraja et al., 2014
k_α	$[7 \times 10^{-7}, 8.3 \times 10^{-6}]$	8.3×10^{-6}	ng/cells/day	Nagaraja et al., 2014; Wang et al., 2012
d_α	$[12.79, 55]$	12.79	1/day	Nagaraja et al., 2014; Wang et al., 2012
a_{pm}	$[0.01, 3.162]$	3.162	ng/mL	Kojouharov et al., 2017; Lacey et al., 2009
a_{mb}	$[0.1, 10]$	0.1	ng/mL	Kojouharov et al., 2017; Lacey et al., 2009
a_{pb}	$[10, 50]$	10	ng/mL	Kojouharov et al., 2017; Lacey et al., 2009
a_{pm_1}	$[5, 13]$	13	ng/mL	Bastidas-Coral et al., 2016; Kojouharov et al., 2017
k_{pm}	$[0.5, 1.01]$	0.5	1/day	Bailon-Plaza and Van Der Meulen, 2001; Isaksson et al., 2008
d_m	$[0.3, 1]$	1	1/day	Bailon-Plaza and Van Der Meulen, 2001; Isaksson et al., 2008
k_{pb}	$[0.2, 0.35]$	0.2202	1/day	Bailon-Plaza and Van Der Meulen, 2001; Isaksson et al., 2008
d_b	$[0.1, 0.15]$	0.15	1/day	Bailon-Plaza and Van Der Meulen, 2001; Isaksson et al., 2008
p_{cs}	$[2 \times 10^{-7}, 3 \times 10^{-6}]$	5×10^{-7}	g/cells/day	Bailon-Plaza and Van Der Meulen, 2001; Trejo et al., 2019b
q_{cd_1}	$[2 \times 10^{-7}, 3 \times 10^{-6}]$	5×10^{-7}	mL/cells/day	Bailon-Plaza and Van Der Meulen, 2001; Trejo et al., 2019b
q_{cd_2}	$[2 \times 10^{-8}, 2 \times 10^{-6}]$	8×10^{-8}	mL/cells/day	Bailon-Plaza and Van Der Meulen, 2001; Trejo et al., 2019b
p_{bs}	$[2 \times 10^{-8}, 2 \times 10^{-7}]$	5×10^{-8}	g/cells/day	Bailon-Plaza and Van Der Meulen, 2001; Trejo et al., 2019b
q_{bd}	$[2 \times 10^{-8}, 2 \times 10^{-7}]$	5×10^{-8}	mL/cells/day	Bailon-Plaza and Van Der Meulen, 2001; Trejo et al., 2019b
K_{lb}	$[2.7 \times 10^4, 1 \times 10^6]$	1×10^6	cells/mL	Bailon-Plaza and Van Der Meulen, 2001; Isaksson et al., 2008
K_{lm}	$[1 \times 10^5, 1 \times 10^6]$	1×10^6	cells/mL	Bailon-Plaza and Van Der Meulen, 2001; Tevlin et al., 2017
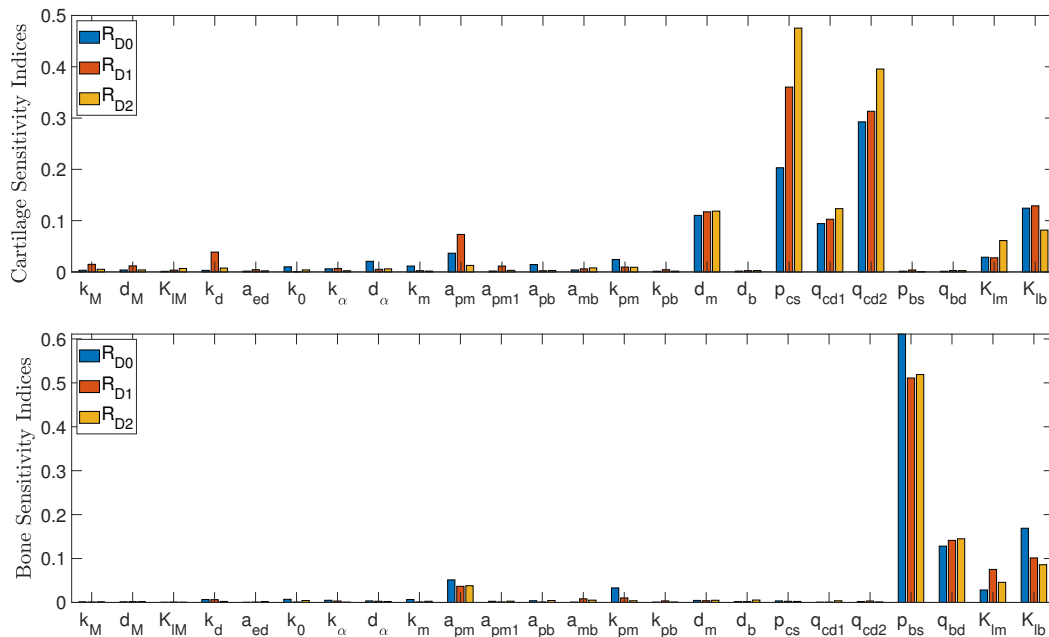
Figure 4: Sensitivity analysis results for cartilage and bone densities using different phagocytic rates, R_D. The most influential parameters to the variability in the cartilage outcome are p_{cs} and q_{cd2} (top), while for the bone outcome is p_{bs} (bottom).
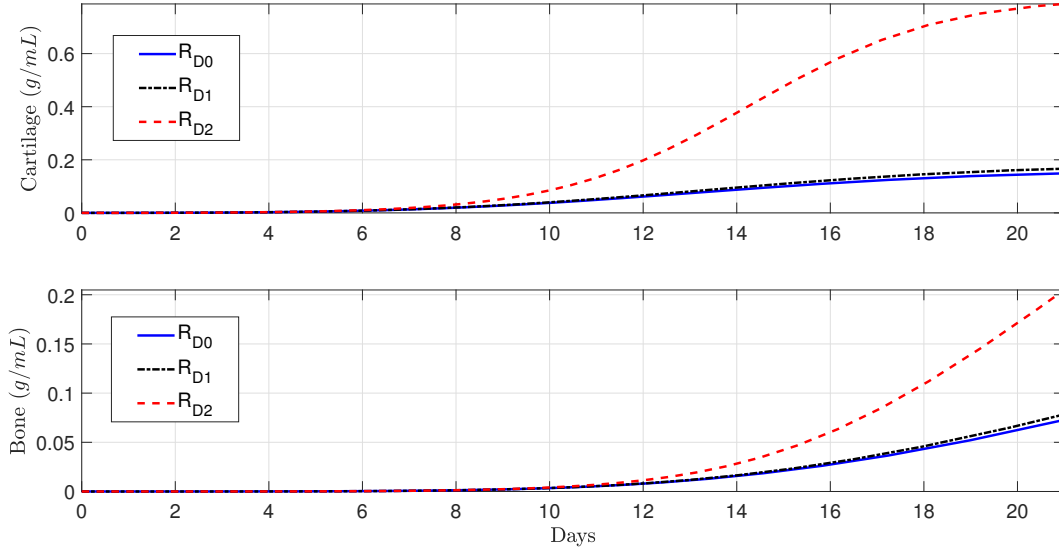
Figure 5: Tissues evolution in a small fracture under the effects of different phagocytic rates, R_D. The slower phagocytic rate R_{D2} yields higher production of both tissues rather than the faster phagocytic rates R_{D1} and R_{D0}, after 8 and 12 days, respectively.

First, a set of numerical simulation results is presented to investigate the phagocytosis effects on the bone fracture healing process. Next, numerical simulations are performed to analyze the effects of macrophages and TNF-α influx rates on the fibrocartilage and the bone densities under both normal and pathological conditions. Another set of numerical simulations is performed to study the influence of the MSCs migration rate on the tissues progression. All simulations are performed until day 21, which is the elapsed time for the inflammatory and repair phases of bone fracture healing process in mice (Einhorn and Gerstenfeld, 2015; Trejo et al., 2019b). The simulations are obtained by using the adaptive MATLAB® solver ode23tb, with initial conditions equal to zero, except for the initial debris densities being set to $D(0) = 5 \times 10^7$.

6.1   Phagocytosis effects on the bone fracture healing process

During the inflammatory phase, macrophage capacity to engulf necrotic cells and unwanted material contributes with the resolution of inflammation (Baht et al., 2018; Elliott et al., 2017). However, the exact effects of phagocytosis on the entire bone fracture healing process is not clearly understood (Elliott et al., 2017; Sinder et al., 2015). In this section, Model (1)–(7) is used to investigate how the fibrocartilage and woven bone densities evolve under the three different phagocytic rates R_{D0}, R_{D1}, and R_{D2}. In the different sets of numerical simulations, the initial debris densities are chosen to be below ($D(0) = 5 \times 10^5$), equal to ($D(0) = 4.71 \times 10^6$), and above ($D(0) = 5 \times 10^8$) the half-saturation of debris, a_{ed}, which represent small, moderate, and severe fractures, respectively (Trejo et al., 2019b).

Figure 5 shows the numerical evolution of the tissues' production/degradation for the different phagocytic rates within a small fracture, $D(0) = 5 \times 10^5$. The evolution of the cartilage and bone behave very similarly over time when using the model with phagocytic rates R_{D0} and R_{D1}, while their densities are more than doubled after the first week and beyond, when using the phagocytic rate R_{D2}. By construction, the phagocytic rates satisfy $R_{D2} < R_{D1} < R_{D0}$ as functions of debris for all $0 < D(t) < D(0) < a_{ed} = 4.71 \times 10^6$. Hence, we observe in Figure 5 that higher tissue productions result under a slower phagocytic rate rather than under faster phagocytic rates, R_{D0} and R_{D1}, after the second week and beyond. This computationally confirms the observed potential role of an early fracture hematoma present at the repair site in enhancing both tissue productions (Kojouharov et al., 2017; Kolar et al., 2010).

Figure 6 shows the numerical evolution of the tissues' production/degradation for the different phagocytic rates within a moderate fracture, i.e., $D(0) = 4.71 \times 10^6$. The evolution of each tissue exhibits similar qualitative behavior under the three phagocytic rates. However, more cartilage synthesis is observed, after four days, with R_{D2} followed by R_{D1} and then R_{D0}, while more bone synthesis is observed, after ten days, with R_{D1} followed by R_{D0} and then R_{D2}. This suggests that the phagocytic rate R_{D1} is the most suitable when modeling the evolution of the two bone tissues for moderate fractures.

Figure 7 shows the numerical evolution of the tissues' production/degradation for the different phagocytic rates within a severe fracture, $D(0) = 5 \times 10^8$. The two tissues densities evolve differently for R_{D0} compered with R_{D1} and R_{D2}. For R_{D0} the cartilage slowly increases in the first few days, it achieves its maximum density around day ten, and then decreases over time;
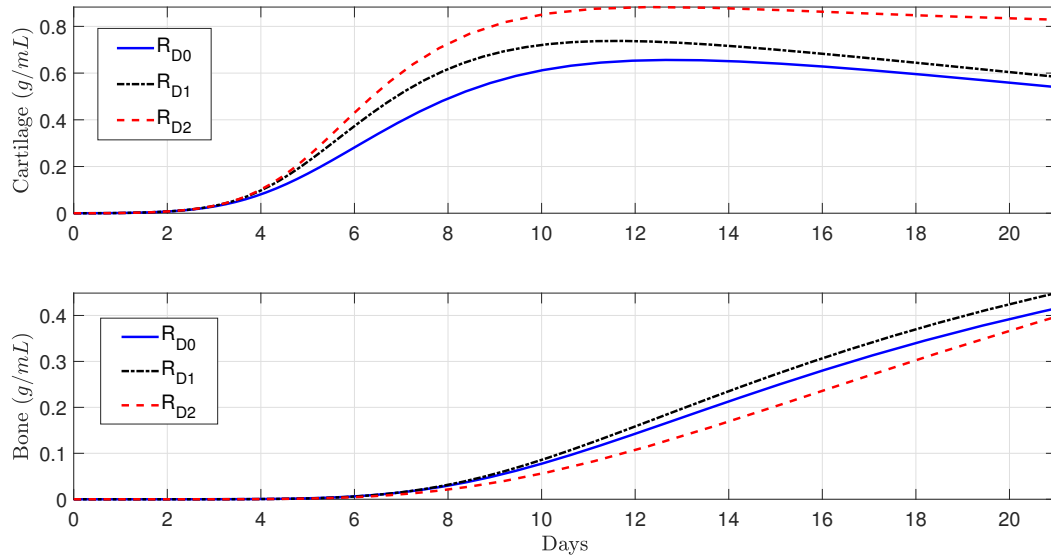
Figure 6: Tissues evolution in a moderate fracture under the effects of different phagocytic rates, R_D. More cartilage synthesis is observed, after 4 days, with R_{D2} followed by R_{D1} and then R_{D0}, while more bone synthesis is observed, after one week, with R_{D1} followed by R_{D0} and then R_{D2}.
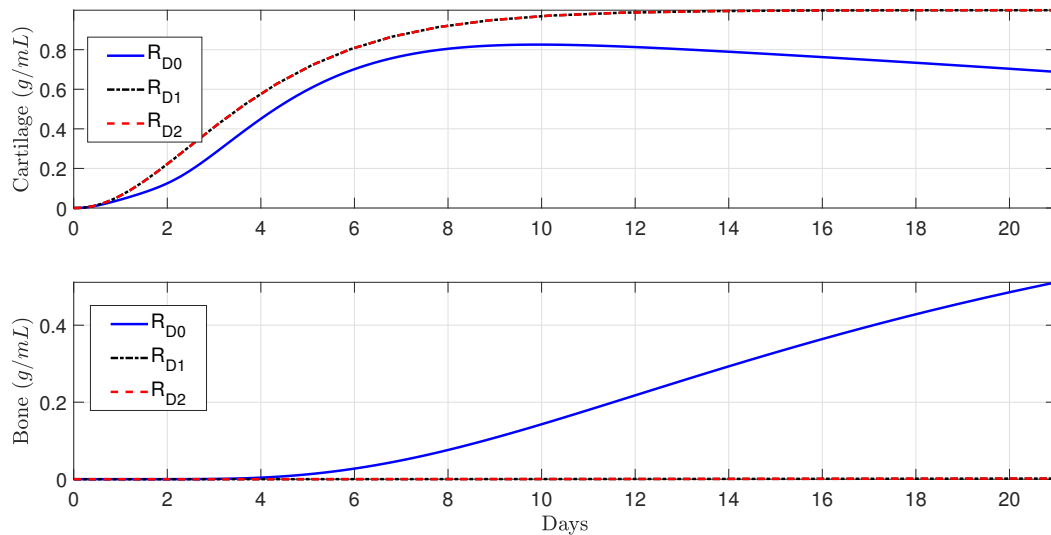

Figure 7: Tissues evolution in a severe fracture under the effects of different phagocytic rates, R_D. The two tissues evolve similarly under the influence of saturated phagocytic rates, R_{D1} and R_{D2}, where the cartilage increases until it achieves maximum density but in the absence of a bone density. For R_{D0} the cartilage slowly increases in the first few days, it achieves its maximum density around day ten, and then decreases over time, while the bone tissue drastically increases after day six and beyond.
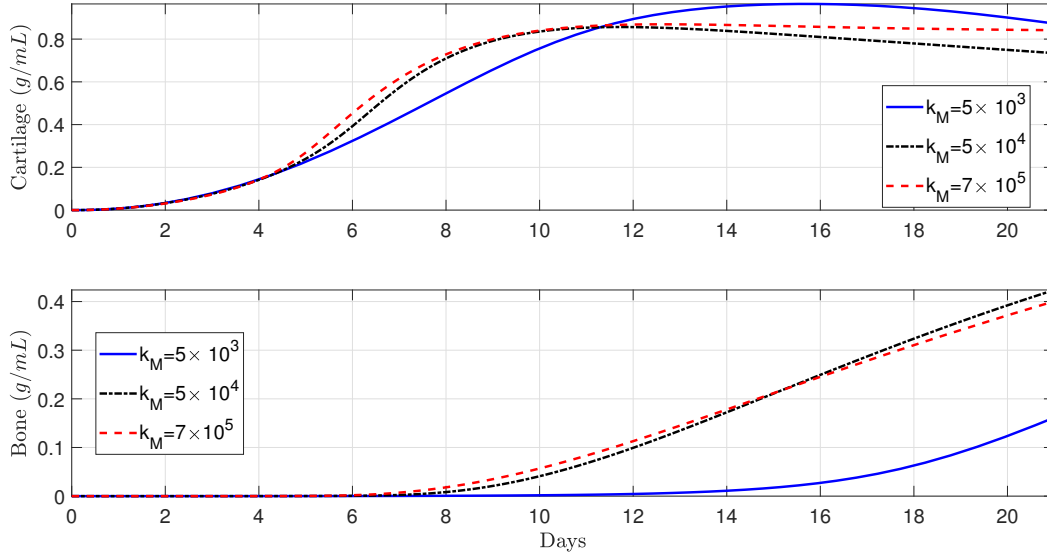
Figure 8: Tissues evolution under the effects of different macrophages migration rates, k_M. Higher cartilage production is observed with the higher macrophages migration rates, 5×10^4 and 7×10^5, between day 5 and day 11, followed by a lower cartilage production under the same migration rates. However, higher bone tissues are produced under faster macrophages migration rates after day 8.

while the bone tissue drastically increases after day six and beyond. For the phagocytic rates given by R_{D1} and R_{D2}, the two tissues evolve similarly, where the cartilages increase until they achieve their maximum densities but in the absence of bone densities. By construction, the phagocytic rate R_{D0} is bigger than R_{D1} and R_{D2}, in severe fractures during the early stages of the bone healing process. Hence, Figure 7 suggests that, in severe fractures, enhancing the clearing of debris by phagocytes is a viable therapeutic interventions to accelerate removal of cartilage and increase bone production.

6.2   Macrophages migration and inflammatory cytokine production effects on the bone fracture healing process

Impairment of bone fracture healing are commonly observed in severe traumas, aging, and immune-compromised individuals, where recruitment of inflammatory cells and cytokine synthesis are locally disturbed at the fracture site (Loi et al., 2016; Mangum et al., 2019; Recknagel et al., 2013). The TNF-α secretion by macrophages significantly increases in older people (Gibon et al., 2016; Loi et al., 2016), while the macrophages influx is reduced in severe fractures (Recknagel et al., 2013). Prolonged and higher inflammatory cells influx are observed during systemic and chronic inflammation (Gibon et al., 2017; Marsell and Einhorn, 2011). Therefore, Model (1)–(7) is used to investigate the effects of different rate values of macrophages migration and TNF-α production, k_M and k_α, on the bone fracture healing process. The values of k_M are set equal to 5×10^3, 5×10^4, and 7×10^5, while the values of k_α are set equal to 8.3×10^{-7}, 8.3×10^{-6}, and 8.3×10^{-5}. All the following simulations are performed under the phagocytic rate R_{D1}, since it is one of the most widely used forms in the literature (Gesztelyi et al., 2012; Trejo et al., 2019b) and, according to our previous numerical results, it is also one of the most suitable form to use in moderate fractures.

Figure 8 shows the numerical evolution of the tissues' production/degradation under the effects of different macrophages migration rates, k_M. The different parameter values of k_M lead to changes in the two tissue densities. When using the smallest value of $k_M = 5 \times 10^3$, less bone formation is observed, while the cartilage density is the smallest between day 5 and day 11, then it increases and achieves its maximum value at day 16, before being degraded. When using $k_M = 5 \times 10^4$ and $k_M = 7 \times 10^5$ both cartilage densities have similar behaviours until day 11, after which the cartilage is been degraded when using $k_M = 5 \times 10^4$ while the cartilage density does not change when $k_M = 7 \times 10^5$. In this simulation, the parameter $k_M = 7 \times 10^5$ was selected such that the inequality $k_\alpha k_M > d_\alpha d_M$ holds, which corresponds to the dashed curves in Figure 8 representing the evolution of an unsuccessful healing with a chronic inflammation, Theorem 4.

Figure 9 shows the numerical evolution of the tissues' production/degradation under the effects of different T_α secretion rates, k_α. The different parameter values of k_α lead to drastic changes in both tissue densities, after the first week and beyond. For the cartilage, higher production of TNF-α results in greater synthesis of cartilage, while the opposite effect is observed with
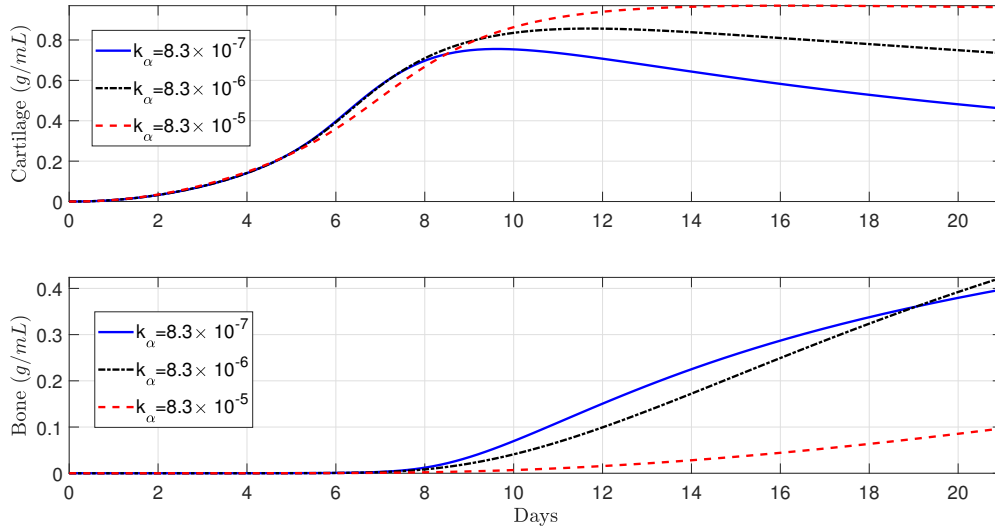
Figure 9: Tissues evolution under the effects of different TNF-α secretion rates, k_α. Higher production of TNF-α results in greater synthesis of cartilage, after day 10, while an opposite effect is observed with the bone production.

the bone. In addition, cartilage degradation is not observed for the larger values of k_α.

6.3 MSCs migration effects on the bone fracture healing process

In this section, Model (1)–(7) is used to study the impact of the MSCs migration rate, k_m, on the bone fracture healing process by observing the cartilage and bone evolution.

Figure 10 shows the numerical evolution of the tissues' production/degradation under the effects of different MSCs migration rates, k_m. As seen in the figure, different parameter values of k_m lead to drastic changes in the cartilage densities within the first two weeks, while there are no significant differences in the bone densities over time. The cartilage synthesis increases as the MSCs migration rate increases, suggesting that an early cartilage production can be accelerated by enhancing MSCs recruitment.

7 Discussion and Conclusions

A novel mathematical model was introduced to study the fundamental functions of phagocytes and inflammatory cytokines during the bone fracture healing process. The major contribution of our model is the formation of a theoretical framework that expands previous mathematical models (Bailon-Plaza and Van Der Meulen, 2001; Kojouharov et al., 2017; Trejo et al., 2019a,b) by considering a general phagocytic rate function of debris removal by macrophages, and by explicitly incorporating the role of the pro-inflammatory cytokines in the process of cellular migration during bone fracture healing. The model analysis revealed that excessive accumulation of phagocytes and inflammatory cytokines at the injury site can lead to unsuccessful fracture healing, while the numerical simulations showed that optimal healing outcomes depend on the abilities of the phagocytes to efficiently engulf debris.

The stability analysis of the model showed the full range of possible different healing outcomes, including successful healing, and delayed and nonunion healing with or without resolved inflammation (Theorems 1–4). In addition, a series of rate inequalities were derived from the stability analysis (Table 3). These inequalities indicate which one of all possible states will occur in the long-term healing process, and therefore, can be useful in clinical evaluations for classification and prediction of the different bone fracture healing outcomes. Accordingly, successful healing, E_1, is achieved when macrophages and TNF-α do not accumulate at the injury site, $k_\alpha k_M > d_\alpha d_M$, mesenchymal stem cells differentiate faster than they proliferate, $d_m > k_{pm}$, while osteoblasts have an opposite mechanistic differentiation-proliferation, $k_{pb} > d_b$.

The bifurcation analysis provided further insight into how the equilibria of the system, their number and properties, depend on the model parameters. By perturbing the values of the parameters representing the proliferation rate of MSCs, k_{pm}, and the migration rate of macrophages, k_M, the bifurcation plots showed that the successful healing state E_1 changes its stability properties at two different bifurcation points, Figures 2 and 3. This implied that the bone fracture healing process will result either in a delayed or nonunion healing with and without chronic inflammation responses, respectively. In addition, the perturbation of
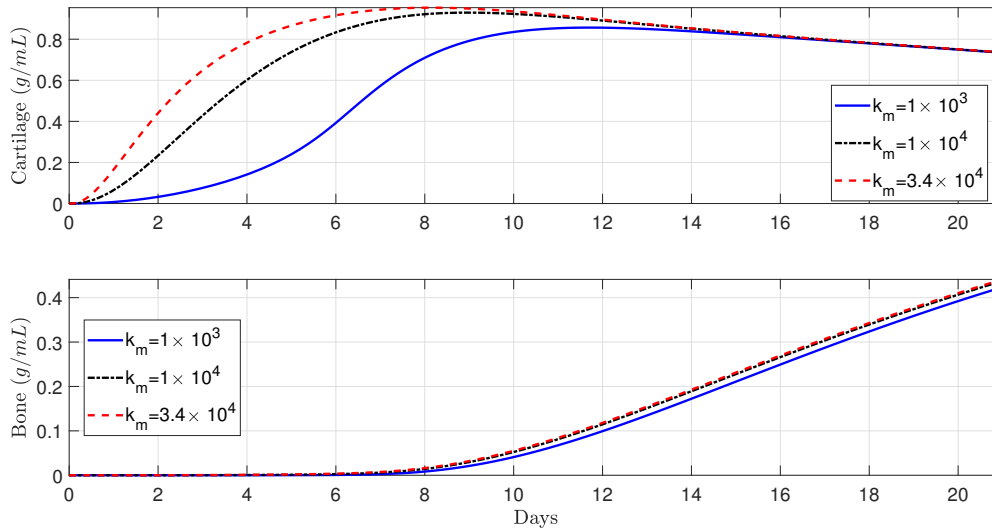
Figure 10: Tissues evolution under the effects of different MSCs migration rates, k_m. Faster MSCs migration leads earlier cartilage production, while there are no significant differences in the bone densities over time.

these two parameter values showed the different scenarios on equilibria sets that System (1)–(7) has, confirming the theoretical results from the stability analysis.

The sensitivity analysis revealed that the most influential parameters on the variability of the model outputs are the production and degradation rates of the two tissues, with the cartilage production and degradation rates accounting for more than 20% of the total cartilage variance per each parameter, while the bone tissue production rate accounting for more than 60% of the total bone variance density.

The numerical simulations showed that different types of phagocytic rates can lead to a very different short-term tissues evolution. It was observed that, in severe fractures, when phagocytosis is modeled by a saturation-rate function it results in a delay in both cartilage degradation and bone synthesis, while normal healing progression is observed when using a linear rate function to represent phagocytosis. These results suggest that optimal healing outcomes may depend on the ability of phagocytes to successfully remove debris. The numerical simulations also confirmed that the early fracture hematoma formation, present at the repair site, enhances both tissues productions in small fractures (Kolar et al., 2010). Additionally, it was observed that, after the first week of the healing process, low macrophages migration rates and high pro-inflammatory cytokines production by macrophages lead to an increase in cartilage synthesis while restricting the bone formation. Also, the numerical simulations showed that higher MSCs migration rates can lead to higher cartilage production. Those findings suggest that an increase of MSCs recruitment can be a viable therapeutic intervention that results in an accelerated cartilage formation during the early stages of the bone fracture healing process.

The presented mathematical model can be easily adapted and used to investigate the impact of a variety of different events that occur during bone fracture healing, which can in turn guide future laboratory experiments and help to explore possible therapeutic procedures that prevent and accelerate the healing process. Future research directions include modifications of the model by incorporating spatial effects to account for cellular migration by chemotaxis and the integration of chondrocytes, osteoclasts, and other molecular factors such as anti-inflammatory cytokines, which also regulate the bone fracture healing process.

References

Arango Duque, G. and A. Descoteaux (2014). Macrophage cytokines: involvement in immunity and infectious diseases. *Frontiers in immunology 5*, 491. 172, 174, 176

Baht, G. S., L. Vi, and B. A. Alman (2018). The role of the immune cells in fracture healing. *Current osteoporosis reports 16*(2), 138–145. 171, 172, 173, 182

Bailon-Plaza, A. and M. C. Van Der Meulen (2001). A mathematical framework to study the effects of growth factor influences on fracture healing. *Journal of Theoretical Biology 212*(2), 191–209. 172, 173, 174, 176, 180, 181, 185

Bastidas-Coral, A. P., A. D. Bakker, B. Zandieh-Doulabi, C. J. Kleverlaan, N. Bravenboer, T. Forouzanfar, and J. Klein-Nulend (2016). Cytokines tnf-*α*, il-6, il-17f, and il-4 differentially affect osteogenic differentiation of human adipose stem cells. *Stem Cells International 2016*, 9 pages. 174, 176, 181

Carlier, A., L. Geris, J. Lammens, and H. Van Oosterwyck (2015). Bringing computational models of bone regeneration to the clinic. *Wiley Interdisciplinary Reviews: Systems Biology and Medicine 7*(4), 183–194. 171

Carlier, A., L. Geris, N. van Gastel, G. Carmeliet, and H. Van Oosterwyck (2015). Oxygen as a critical determinant of bone fracture healing—a multiscale model. *Journal of theoretical biology 365*, 247–264. 174

Dunster, J. L., H. M. Byrne, and J. R. King (2014). The resolution of inflammation: a mathematical model of neutrophil and macrophage interactions. *Bulletin of mathematical biology 76*(8), 1953–1980. 172, 175, 176

Echeverri, L., M. Herrero, J. Lopez, and G. Oleaga (2015). Early stages of bone fracture healing: formation of a fibrin–collagen scaffold in the fracture hematoma. *Bulletin of mathematical biology 77*(1), 156–183. 172

Einhorn, T. A. (2005). The science of fracture healing. *Journal of orthopaedic trauma 19*(10), S4–S6. 172

Einhorn, T. A. and L. C. Gerstenfeld (2015). Fracture healing: mechanisms and interventions. *Nature Reviews Rheumatology 11*(1), 45. 172, 173, 180, 182

Elliott, M. R., K. M. Koster, and P. S. Murphy (2017). Efferocytosis signaling in the regulation of macrophage inflammatory responses. *The Journal of Immunology 198*(4), 1387–1394. 171, 182

Gesztelyi, R., J. Zsuga, A. Kemeny-Beke, B. Varga, B. Juhasz, and A. Tosaki (2012). The hill equation and the origin of quantitative pharmacology. *Archive for history of exact sciences 66*(4), 427–438. 172, 175, 184

Ghiasi, M. S., J. Chen, A. Vaziri, E. K. Rodriguez, and A. Nazarian (2017). Bone fracture healing in mechanobiological modeling: A review of principles and methods. *Bone Reports 6*, 87–100. 171, 172

Gibon, E., F. Loi, L. A. Córdova, J. Pajarinen, T. Lin, L. Lu, A. Nabeshima, Z. Yao, and S. B. Goodman (2016). Aging affects bone marrow macrophage polarization: relevance to bone healing. *Regenerative engineering and translational medicine 2*(2), 98–104. 184

Gibon, E., L. Y. Lu, K. Nathan, and S. B. Goodman (2017). Inflammation, ageing, and bone regeneration. *Journal of orthopaedic translation 10*, 28–35. 171, 180, 184

Gómez-Barrena, E., P. Rosset, D. Lozano, J. Stanovici, C. Ermthaller, and F. Gerbhard (2015). Bone fracture healing: cell therapy in delayed unions and nonunions. *Bone 70*, 93–101. 171, 172, 173

Isaksson, H. (2012). Recent advances in mechanobiological modeling of bone regeneration. *Mechanics Research Communications 42*, 22–31. 180

Isaksson, H., C. C. van Donkelaar, R. Huiskes, and K. Ito (2008). A mechano-regulatory bone-healing model incorporating cell-phenotype specific activity. *Journal of theoretical biology 252*(2), 230–246. 181

Italiani, P. and D. Boraschi (2014). From monocytes to m1/m2 macrophages: phenotypical vs. functional differentiation. *Frontiers in immunology 5*, 514. 172, 173, 176

Kojouharov, H. V., I. Trejo, and B. M. Chen-Charpentier (2017). Modeling the effects of inflammation in bone fracture healing. *AIP Conference Proceedings 1895*(1), 020005. 171, 172, 173, 174, 176, 181, 182, 185

Kolar, P., K. Schmidt-Bleek, H. Schell, T. Gaber, D. Toben, G. Schmidmaier, C. Perka, F. Buttgereit, and G. N. Duda (2010). The early fracture hematoma and its potential role in fracture healing. *Tissue Engineering Part B: Reviews 16*(4), 427–434. 182, 186

Lacey, D., P. Simmons, S. Graves, and J. Hamilton (2009). Proinflammatory cytokines inhibit osteogenic differentiation from stem cells: implications for bone repair during inflammation. *Osteoarthritis and Cartilage 17*(6), 735–742. 181

Loi, F., L. A. Córdova, J. Pajarinen, T.-h. Lin, Z. Yao, and S. B. Goodman (2016). Inflammation, fracture and bone repair. *Bone 86*, 119–130. 171, 184

Mangum, L. H., J. J. Avila, B. J. Hurtgen, A. L. Lofgren, and J. C. Wenke (2019). Burn and thoracic trauma alters fracture healing, systemic inflammation, and leukocyte kinetics in a rat model of polytrauma. *Journal of orthopaedic surgery and research 14*(1), 58. 171, 184

Marée, A. F., M. Komba, C. Dyck, M. Labkecki, D. T. Finegood, and L. Edelstein-Keshet (2005). Quantifying macrophage defects in type 1 diabetes. *Journal of theoretical biology 233*(4), 533–551. 181

Marino, S., I. B. Hogue, C. J. Ray, and D. E. Kirschner (2008). A methodology for performing global uncertainty and sensitivity analysis in systems biology. *Journal of theoretical biology 254*(1), 178–196. 180

Marsell, R. and T. A. Einhorn (2011). The biology of fracture healing. *Injury 42*(6), 551–555. 172, 173, 180, 184

M'Barek, K. B., D. Molino, S. Quignard, M.-A. Plamont, Y. Chen, P. Chavrier, and J. Fattaccioli (2015). Phagocytosis of immunoglobulin-coated emulsion droplets. *Biomaterials 51*, 270–277. 172, 175

Michalski, M. N., A. J. Koh, S. Weidner, H. Roca, and L. K. McCauley (2016). Modulation of osteoblastic cell efferocytosis by bone marrow macrophages. *Journal of cellular biochemistry 117*(12), 2697–2706. 171

Mountziaris, P. M. and A. G. Mikos (2008). Modulation of the inflammatory response for enhanced bone tissue regeneration. *Tissue Engineering Part B: Reviews 14*(2), 179–186. 172

Nagaraja, S., A. Wallqvist, J. Reifman, and A. Y. Mitrophanov (2014). Computational approach to characterize causative factors and molecular indicators of chronic wound inflammation. *The Journal of Immunology 192*(4), 1824–1834. 181

Newman, S. L., J. E. Henson, and P. M. Henson (1982). Phagocytosis of senescent neutrophils by human monocyte-derived macrophages and rabbit inflammatory macrophages. *Journal of Experimental Medicine 156*(2), 430–442. 173, 174, 181

Otto, S. P. and T. Day (2011). *A biologist's guide to mathematical modeling in ecology and evolution*. Princeton University Press. 177

Pajarinen, J., T. Lin, E. Gibon, Y. Kohno, M. Maruyama, K. Nathan, L. Lu, Z. Yao, and S. B. Goodman (2019). Mesenchymal stem cell-macrophage crosstalk and bone healing. *Biomaterials 196*, 80–89. 171, 172

Pisani, P., M. D. Renna, F. Conversano, E. Casciaro, M. Di Paola, E. Quarta, M. Muratore, and S. Casciaro (2016). Major osteoporotic fragility fractures: Risk factor updates and societal impact. *World journal of orthopedics 7*(3), 171. 171

Pivonka, P. and C. R. Dunstan (2012). Role of mathematical modeling in bone fracture healing. *BoneKEy reports 1*, 221. 171, 172, 180

Recknagel, S., R. Bindl, C. Brochhausen, M. Göckelmann, T. Wehner, P. Schoengraf, M. Huber-Lang, L. Claes, and A. Ignatius (2013). Systemic inflammation induced by a thoracic trauma alters the cellular composition of the early fracture callus. *Journal of Trauma and Acute Care Surgery 74*(2), 531–537. 171, 184

Reynolds, A., J. Rubin, G. Clermont, J. Day, Y. Vodovotz, and G. B. Ermentrout (2006). A reduced mathematical model of the acute inflammatory response: I. derivation of model and analysis of anti-inflammation. *Journal of theoretical biology 242*(1), 220–236. 172, 175

Ricciotti, E. and G. A. FitzGerald (2011). Prostaglandins and inflammation. *Arteriosclerosis, thrombosis, and vascular biology 31*(5), 986–1000. 172

Saltelli, A., S. Tarantola, and K. P.-S. Chan (1999). A quantitative model-independent method for global sensitivity analysis of model output. *Technometrics 41*(1), 39–56. 180

Schell, H., G. Duda, A. Peters, S. Tsitsilonis, K. Johnson, and K. Schmidt-Bleek (2017). The haematoma and its role in bone healing. *Journal of experimental orthopaedics 4*(1), 5. 171

Schlundt, C., T. El Khassawna, A. Serra, A. Dienelt, S. Wendler, H. Schell, N. van Rooijen, A. Radbruch, R. Lucius, S. Hartmann, et al. (2018). Macrophages in bone fracture healing: their essential role in endochondral ossification. *Bone 106*, 78–89. 171

Schlundt, C., H. Schell, S. B. Goodman, G. Vunjak-Novakovic, G. N. Duda, and K. Schmidt-Bleek (2015). Immune modulation as a therapeutic strategy in bone regeneration. *Journal of experimental orthopaedics 2*(1), 1. 173

Schmidt-Bleek, K., B. J. Kwee, D. J. Mooney, and G. N. Duda (2015). Boon and bane of inflammation in bone tissue regeneration and its link with angiogenesis. *Tissue Engineering Part B: Reviews 21*(4), 354–364. 172

Serhan, C. N. and J. Savill (2005). Resolution of inflammation: the beginning programs the end. *Nature immunology 6*(12), 1191–1197. 172, 174

Sherratt, J. A. and J. Murray (1990). Models of epidermal wound healing. *Proc. R. Soc. Lond. B 241*(1300), 29–36. 176

Sinder, B. P., A. R. Pettit, and L. K. McCauley (2015). Macrophages: their emerging roles in bone. *Journal of Bone and Mineral Research 30*(12), 2140–2149. 171, 182

Strang, G., G. Strang, G. Strang, and G. Strang (1993). *Introduction to linear algebra*, Volume 3. Wellesley-Cambridge Press Wellesley, MA. 177

Stuart, A. and A. R. Humphries (1998). *Dynamical systems and numerical analysis*, Volume 2. Cambridge University Press. 176, 178

Swirski, F. K., I. Hilgendorf, and C. S. Robbins (2014). From proliferation to proliferation: monocyte lineage comes full circle. In *Seminars in immunopathology*, Volume 36, pp. 137–148. Springer. 174

Tevlin, R., E. Y. Seo, O. Marecic, A. McArdle, X. Tong, B. Zimdahl, A. Malkovskiy, R. Sinha, G. Gulati, X. Li, et al. (2017). Pharmacological rescue of diabetic skeletal stem cell niches. *Science translational medicine 9*(372), eaag2809. 181

Torres, M., J. Wang, P. J. Yannie, S. Ghosh, R. A. Segal, and A. M. Reynolds (2019). Identifying important parameters in the inflammatory process with a mathematical model of immune cell influx and macrophage polarization. *PLoS computational biology 15*(7), e1007172. 175

Trejo, I., H. Kojouharov, and B. Chen-Charpentier (2019a). Modeling the effects of growth factors on bone fracture healing. In *AIP Conference Proceedings*, Volume 2164:1, pp. 020003. AIP Publishing LLC. 171, 172, 185

Trejo, I., H. Kojouharov, and B. Chen-Charpentier (2019b). Modeling the macrophage-mediated inflammation involved in the bone fracture healing process. *Mathematical and Computational Applications 24*(1), 12. 171, 172, 173, 174, 175, 176, 180, 181, 182, 184, 185

Trejo, I. and H. V. Kojouharov (2019). Understanding the fundamental molecular mechanism of osteogenic differentiation from mesenchymal stem cells. *Applications & Applied Mathematics 14*(2), 678–698. 171

Ullah, M., J. Eucker, M. Sittinger, and J. Ringe (2013). Mesenchymal stem cells and their chondrogenic differentiated and dedifferentiated progeny express chemokine receptor ccr9 and chemotactically migrate toward ccl25 or serum. *Stem cell research & therapy 4*(4), 99. 172, 173, 174, 176, 181

Van Furth, R., M. M. Diesselhoff-den Dulk, and H. Mattie (1973). Quantitative study on the production and kinetics of mononuclear phagocytes during an acute inflammatory reaction. *Journal of experimental medicine 138*(6), 1314–1330. 181

Van Zon, J. S., G. Tzircotis, E. Caron, and M. Howard (2009). A mechanical bottleneck explains the variation in cup growth during fcγr phagocytosis. *Molecular systems biology 5*(1), 298. 172

Wang, Y., T. Yang, Y. Ma, G. V. Halade, J. Zhang, M. L. Lindsey, and Y.-F. Jin (2012). Mathematical modeling and stability analysis of macrophage activation in left ventricular remodeling post-myocardial infarction. *BMC genomics 13*(6), S21. 181

Wiggins, S. (2003). *Introduction to applied nonlinear dynamical systems and chaos*, Volume 2. Springer Science & Business Media. 179

Wu, A. C., L. J. Raggatt, K. A. Alexander, and A. R. Pettit (2013). Unraveling macrophage contributions to bone repair. *BoneKEy reports 2*, 373. 171

Yu, T. (2014). *Design and validation of a mathematical model to describe macrophage dynamics in wound healing*. Ph. D. thesis, Drexel University. 181